Journal of Experimental Botany, Vol. 58, No. 4, pp. 839–854, 2007
Imaging Stress Responses in Plants Special Issue
doi:10.1093/jxb/erl237 Advance Access publication 17 January, 2007

Journal of Experimental Botany

SPECIAL ISSUE PAPER

Geophysical imaging of root-zone, trunk, and moisture heterogeneity

Said Attia al Hagrey*

Department of Geophysics, Institute of Geosciences, Kiel University, Otto-Hahn-Platz 1, D-24098 Kiel, Germany

Received 28 May 2006; Accepted 16 October 2006

Abstract

The most significant biotic and abiotic stress agents of water extremity, salinity, and infection lead to wood decay and modifications of moisture and ion content, and density. This strongly influences the (di-)electrical and mechanical properties and justifies the application of geophysical imaging techniques. These are less invasive and have high resolution in contrast to classical methods of destructive, single-point measurements for inspecting stresses in trees and soils. This review presents some *in situ* and *in vivo* applications of electric, radar, and seismic methods for studying water status and movement in soils, roots, and tree trunks. The electrical properties of a root-zone are a consequence of their moisture content. Electrical imaging discriminates resistive, woody roots from conductive, soft roots. Both types are recognized by low radar velocities and high attenuation. Single roots can generate diffraction hyperbolas in radargrams. Pedophysical relationships of water content to electrical resistivity and radar velocity are established by diverse infiltration experiments in the field, laboratory, and in the full-scale 'GeoModel' at Kiel University. Subsurface moisture distributions are derived from geophysical attribute models. The ring electrode technique around trunks images the growth ring structure of concentric resistivity, which is inversely proportional to the fluid content. Healthy trees show a central high resistivity within the dry heartwood that strongly decreases towards the peripheral wet sapwood. Observed structural deviations are caused by infection, decay, shooting, or predominant light and/or wind directions. Seismic trunk tomography also differentiates between decayed and healthy woods.

Key words: Electrical resistivity techniques, radar imaging, ring electrode array, root-zone, sap flow, seismic tomography, trunk ring structure, vadose zone, water content, water flow.

Introduction

The increasing global demand for land use and water in terms of quality and quantity calls for sustainable management of water catchments and better understanding of water and solute movement. The soil and water qualities and proportions greatly affect tree health. Within the research project WATERUSE, the team at Kiel University together with European partners from disciplines of botany, agronomy, and soil hydrology developed integrating techniques for analysing water flow through the soil–plant–atmosphere continuum, adequate for use in heterogeneous stands in dry regions. For example, trees are subjected to biotic and abiotic (physical, anthropogenic, chemical, etc) stresses causing changes in their physiological structures and water relations. These can lead to productivity loss and certainly to damage and decline. Biotic stresses include insect pests and disease problems that lead to decay (integrity/weight loss) of wood tissues in living trees. Depolymerization reduces the mechanical resistance and stability, causing serious economical losses and environmental risks. Water extremes (both deficit and excess) are the most significant abiotic stress agents, followed by those of temperature (hot and cold), chemical pollution (salt and pesticide), oxidative ozone radiation, and mechanical damage, for example, for roots in urban trees. Abiotic stresses can weaken a tree and make it more susceptible to biotic agents. These stresses modify the physical characteristics, strongly influence the electric and mechanical properties, and justify the *in vivo* application of geophysical techniques

* E-mail: sattia@geophysik.uni-kiel.de

(Pellerin *et al*., 1985; Shortle and Smith, 1987; Wilcox, 1988; Beall, 1996; Raczkowski *et al*., 1999).

A range of geophysical tools are appropriate for the detailed study of water movement and of tissue damage in response to various environmental stresses (Tattar and Blanchard, 1976; Shortle, 1982). For example, effective non-destructive evaluation methods for early detection of decay in living trees, especially those that do not have external indicators, would enable identification of stressed and endangered trees, prevent the decay spread, and improve stand conditions.

Conventional instrumental approaches of the widely used visual tree assessment (VTA) method use a commercial impulse hammer, wood penetrometer, and fractometer to measure the electric resistivity ρ and elastic wave velocity v at single sparse points (Mattheck and Breloer, 1994). These are insufficient for spatial detection of wood decay. Recently, more accurate geophysical imaging tomography techniques based on ρ, ε_r (relative dielectric permittivity), v (radar and seismic), attenuation α, and elastic modulus E have been developed for diagnosis of wood moisture content, density, mechanical elasticity, and degradation (Tomikawa *et al*., 1990; Bucur, 1995, 2003; Hagrey *et al*., 2003, 2004).

Geophysical methods image the medium under study in 2D and 3D, and monitor changes and processes in 4D. They offer good parametrical and spatio-temporal resolution combined with a minimally invasive character. Imaging techniques of electric resistivity (DC), ground-penetrating radar (GPR) (from MHz to a few GHz), and seismic (from Hz to tens of kHz), extend their *in situ* application range from hydrogeophysical targets (e.g. static ground and soil water content and dynamic preferential pathways) into the less known *in vivo* investigation of biogeophysical targets of living plants (e.g. root-zone, trunk structure, diagnosing wood decay, and their physiological water processes of redistribution, uptake, and sap) (Hagrey and Michaelsen, 1999, 2002; Hagrey *et al*., 1999, 2003; Hubbard *et al*., 2002; Hanafy and Hagrey, 2006).

This paper presents the background, potential, and some *in vivo* and *in situ* applications of geophysical imaging techniques to the study of water relations in trees and soils. Particular high resolution applications that will be reviewed include: (i) hydrological mapping of vadose soil layers by establishing a pedophysical relationship (transfer function) to invert geophysical attribute models into subsurface moisture distributions; (ii) mapping single roots and the whole root envelope within the unsaturated vadose zone (including interfaces between unsaturated soils and roots); (iii) detecting and localizing decayed wood zones (e.g. bacterial, fungal rots), cavities, or hollows (involving interfaces between healthy and degraded wood); (iv) imaging the internal structure or anatomy of trunks (to resolve the xylem growth rings, the sap–heartwood interface); and (v) exploring the capability to monitor physiological process, for example, sap flow, water uptake by roots, as well as soil water flow.

Materials, methods, and properties

This section generally outlines the nature of the study media (vadose soil, root-zone, and trunk), the background of the applied imaging techniques (geoelectrics, radar, and seismics), and hydro-/pedophysical properties and relationships for deriving moisture content from geophysical attributes (ρ, ε_r, v). The purpose is to understand the geophysical attribute sensitivity for structures and processes and to justify the *in vivo* and *in situ* imaging approaches in studying stresses.

Soil and tree media under study

The complex (composite) study media consist of the three-phase vadose zone (soil grain, water, and air), the four-phase root-zone (grain, organic roots, water, and air—ideally of nearly equal proportions), and the three-phase trunk (water, wood, and air).

Vadose soil and root-zone: This extremely heterogeneous pedosphere regulates the water availability for vegetation and controls the transport of water, solute, and contaminants (e.g. agrochemicals, pesticides) from the ground surface into the underlying fresh water aquifer. Subsurface bedding is a consequence of changes in the grain nature (type, shape, orientation, packing), porosity, amount and type of pore fluid, hydraulic conductivity, and tortuosity (Collinson and Thompson, 1989; Schachtschnabel *et al*., 1989). Roots have the major functions of absorbing water and inorganic nutrients, and of anchoring the plant body to the ground. Growing roots change the soil texture, displace pore water and gas, and increase the porosity. Water balance and the physiological process in soils and plants depend on the water uptake by absorbing roots, subsequent water redistribution and hydraulic lift, sap flow, transpiration, and photosynthesis (Richards and Caldwell, 1987; Caldwell, 1988; Dawson and Pate, 1996; Topp *et al*., 1996; Gisi *et al*., 1997; Caldwell *et al*., 1998).

Trunk structure: A typical trunk consists of the old heartwood in the centre followed by the active sapwood, the peripheral cambium, and the bark of living phloem and dead cork (Miller, 1999; Fig. 1). Sapwoods with concentric annual growth rings of living xylem tissues are generally wetter, lighter, and weaker than heartwoods. Cells and fibres are elongated axially, causing a pronounced anisotropy of physical properties (Skaar, 1988; Bucur, 2003). The trunk structure and health vary with type, age, branching/shooting, subsurface, environment, and climate (LaMarche, 1974; Tkachuck, 1983; Lamb, 1995).

The fungal or bacterial decay attacking heartwoods increases the moisture θ and ion content and reduces the density and lignin content. Wood stability measurements are used to isolate decay of higher ε_r, σ, and α, and lower v values (Skaar, 1988; Sakai *et al*., 1990; Schad *et al*., 1995; Ross *et al*., 1997, 1999; Simpson and TenWolde, 1999; Sandoz *et al*., 2000; Wang *et al*., 2000).

In conclusion, structures and processes in vadose zones and trunks (e.g. growth rings, structural defects, decays, heterogeneities, and mechanical stabilities) are potential targets for geophysical imaging tomography techniques. The presence and activity of roots cause spatio-temporal variations in water content of significant (di-)electric contrasts (ε_r, σ) within the subsurface.

Electrical resistivity method

Electrical (DC) resistivity surveys are accomplished in both the vadose root-zone and tree trunk using four-point electrodes (often stainless steel, sometimes a non-polarizing NaCl gel) (Fig. 2). An

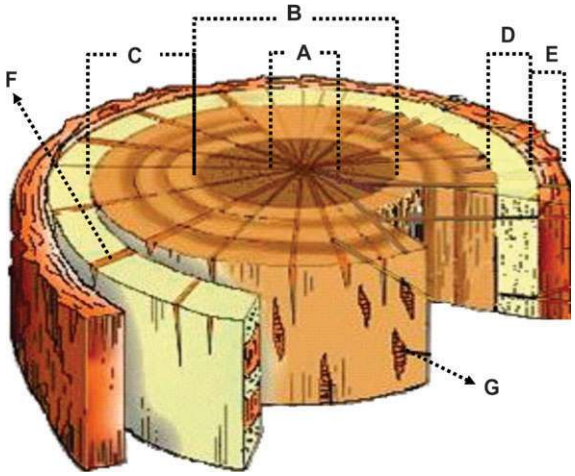

Fig. 1. Cross-section of an oak trunk. (A) Pith, (B) heartwood, (C) sapwood, (D) phloem (living tissue), (E) cork (dry dead tissue), (F) wood rays, and (G) vessel.

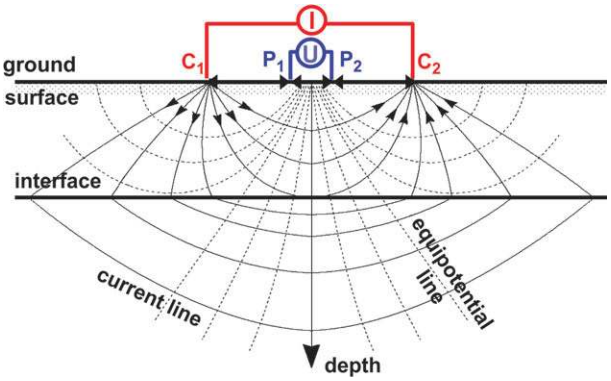

Fig. 2. Four-point electrode configuration in a two-layer model of resistivities ρ_1 and ρ_2. I, current; U, voltage; C, current electrode; P, potential electrode.

electric current I is injected into the medium via a pair of current electrodes (C_1, C_2) and the resulting voltage U is measured between a second pair of potential electrodes (P_1, P_2). The apparent specific electrical resistivity ρ_a (in Ω m, Ω denotes Ohm) over a semi-infinite, heterogeneous, isotropic medium is given by the following equation (Koefoed, 1979; Parasnis, 1997):

$$\rho_a = 2\pi kU/I \quad (1)$$

where k is a geometric factor which depends on the electrode arrangement.

In classical configurations, the Wenner array (C_1, P_1 P_2, C_2) uses equally spaced electrodes, and the dipole–dipole array (C_1, C_2 P_1, P_2) uses the dipole offset (a=C_1–C_2=P_1–P_2) and its n-multiple of the dipole–dipole offset (na=C_2–P_1), (Fig. 3).

The electrical imaging survey is carried out using a distribution of electrodes along individual profiles and grids placed at the outer surface of the study media. The electrode spacing and number depend on the medium size and the resolution required. The concept of constructing an apparent resistivity pseudosection for a 2D survey shows that for each measurement a survey level and lateral position of the array midpoint is determined, and the apparent resistivity

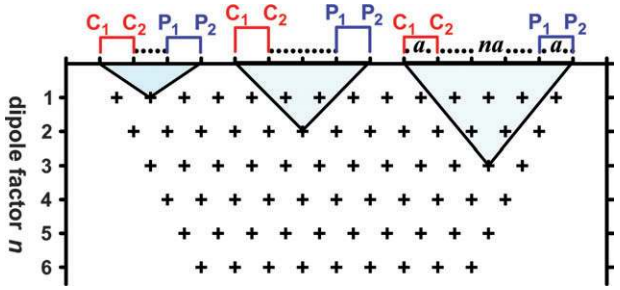

Fig. 3. Acquisition of a 2D apparent resistivity pseudosection using a dipole–dipole array (C_1 C_2 P_1 P_2). C, current electrode; P, potential electrode; a, dipole spacing; n, dipole factor.

ρ_a assigned to that position (Fig. 3) (Hallof, 1957; Dahlin, 1996; Lowrie, 1997). Here, each survey level corresponds to a different electrode spacing. As the spacing increases, the effective penetration depth increases. The pseudosection shows a qualitative image of the subsurface distribution of resistivity. The resulting continuous distribution of a ρ_a data set is inverted into 2D or 3D subsurface models of true resistivity ρ using complex inversions (Loke and Barker, 1995, 1996). Their relationships are solved iteratively using finite element and finite difference algorithms. The inversion starts by calculating forward ρ_a values from an initial (homogeneous or arbitrary) ρ distribution in the study medium. The root mean square misfit between calculated and measured ρ_a is computed and the initial ρ model is corrected accordingly. These steps are repeated iteratively until the misfit converges below a pre-defined threshold value, for example the average data error.

Most soils and woods of very high ρ matrix conduct electricity via the electrolytes of the interstitial or tissue water (Fig. 4; Keller and Frischknecht, 1966; Skaar, 1988). The electric resistivity ρ decreases with increasing pore or cell water content θ, salinity (ion content and mobility), and hydraulic conductivity, as well as temperature (that reduces the viscosity and increases the ion mobility).

Ground-penetrating radar (GPR)

The radar technique uses high frequency f pulsed electromagnetic waves (f=10–2000 MHz) to image the medium under investigation and to characterize its properties. The GPR wave propagation in a medium is mainly controlled by dielectric permittivity ε, electrical conductivity σ (inverse resistivity ρ), and magnetic permeability μ. Most dry soils and woods are nearly non-magnetic and non-conductive media, i.e. of negligible μ and σ at high GPR frequencies. In such low-loss media, the velocity v and wave attenuation α are simply given by the following (Annan, 2004; Neal, 2004):

$$v \approx c/\sqrt{\varepsilon_r} \quad (2)$$

$$\alpha = \frac{1}{\delta} = \frac{\sigma}{2}\sqrt{\mu/\varepsilon}, \quad (3)$$

where c=vacuum velocity (0.3 m ns^{-1}), ε_r=relative dielectric permittivity, and μ_r=relative magnetic permeability (with respect to those of the vacuum, respectively), δ=skin depth; the distance through which a wave amplitude decreases by a factor of exp^{-1} (or 37%).

At an ε_r discontinuity, radar waves propagating from the transmitter Tx are partly reflected and diffracted back to the surface and recorded by the receiver Rx (Fig. 5). For vertical incidence, the

reflected energy amplitude with respect to the total signal amplitude is given by the reflection coefficient R:

$$R \approx \frac{\sqrt{\varepsilon_{r1}} - \sqrt{\varepsilon_{r2}}}{\sqrt{\varepsilon_{r1}} + \sqrt{\varepsilon_{r2}}} = \frac{v_2 - v_1}{v_2 + v_1} \quad (4)$$

Obviously, the GPR wave propagation in low-loss media is dominated by their ε_r and σ. Water has a very high ε_r (81) relative to those of the other constituents of the soil and wood media, where ε_r is 1 for air, $\leqslant 7$ for dry sandy or loamy soils, and 4.5 for dry woods, (Table 1) (Davis and Annan, 1989). Consequently, the water content θ is the most dominating factor in dielectric properties, and its rise increases both ε_r and σ, resulting in decreasing v and increasing α (Topp *et al*., 1980; Olhoeft, 1987). Introducing salt water strongly increases σ and α, and, consequently, decreases the penetration depth (or δ) of the radar waves (Wensink, 1993; Hagrey and Müller, 2000). Single roots as well as interfaces between unsaturated soils and wet root-zone, heart- and sapwood or healthy and decayed woods are potential targets of (di-)electric contrast for radar reflections. Among geophysical techniques, radar has the highest f (lowest wavelength λ, $\lambda = v/f$) and resolution for detecting small and close targets, but also the highest α that limits resolution and penetration in wet conducting media.

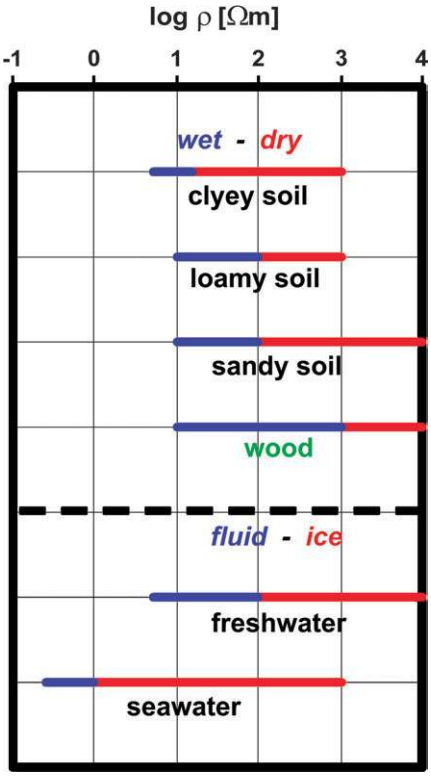

Fig. 4. The resistivity ρ of soils and woods (Keller and Frischknecht, 1976; Skaar, 1988).

Radar imaging surveys are carried out mainly by measuring travel times in the reflection and transmission (tomography) modes. The data acquisition in reflection profiling is often conducted in the single (common) Tx–Rx offset mode (Fig. 5). A radar wave is transmitted, received, and recorded each time the antenna has been moved a fixed distance across any material under investigation. The tomography data are collected where Tx and Rx can be put on opposite sides of a medium to image the volume between the measurement points, for example, between boreholes (crossholes) and between a borehole and the ground surface.

Seismic method

Seismic and ultraseismic body waves (f= from a few Hz to tens of kHz) propagating inside the medium consist of the longitudinal P- and transversal S-waves with a particle motion parallel and perpendicular to the propagation direction, respectively. The waves for soil and wood surveys are generated by a hammer or pulse generator and recorded by a piezoelectric accelerometer or receiver after propagating in the medium under investigation. The recorded travel time is used to calculate the wave velocity v which is given for homogeneous, isotropic media, by the following equation (Telford *et al*., 1990):

$$v = \sqrt{E/d} \quad (5)$$

where d=density, E=elastic modulus which includes the bulk k_b and shear μ_s moduli for the P-wave and only μ_s for the S-wave. In fluids (with $\mu_s = 0$), the S-wave propagation vanishes and the P-wave velocity depends only on k_b (v=1500 m s^{-1}).

Seismic methods are applied to study mechanical stability and detect the decay in trees using tomographic measurements from a series of sensors placed around the trunk perimeter. In living trees and green wood of high moisture content, seismic P-waves are more

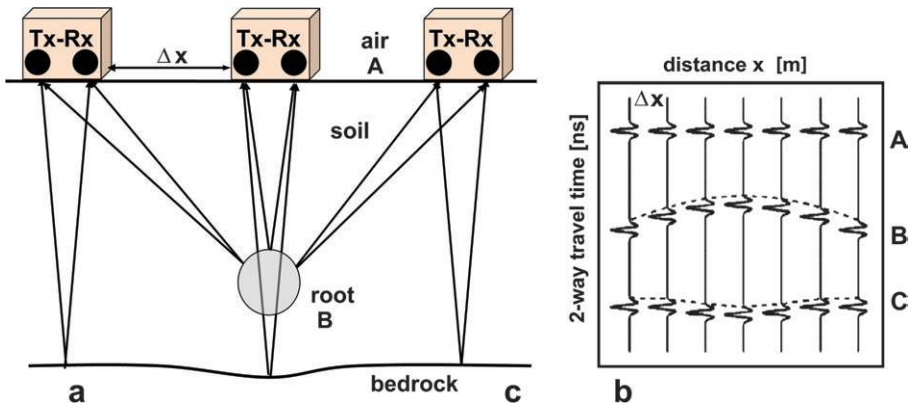

Fig. 5. (a) Radar reflection profiling with a fixed transmitter Tx–receiver Rx offset over an anomalous root and bedrock. (b) Recorded radargram. A, air waves; B, single root reflector; C, bedrock reflections.

Table 1. *Dielectric characteristics of common materials at a GPR frequency of 10–1000 MHz (Daniels, 1996; Asprion, 1998; Torgovnikov, 1993)*

Material	State[a]	ε_r[a]	σ (mS m^{-1})[a]	v (m ns^{-1})[a]	α (dB m^{-1})[a]
Sandy–loamy soil	Dry	4–7	0.1–100	0.11–0.18	0.01–0.1
	Wet	15–30	10–1000	0.05–0.09	0.03–0.3
Wood cellulose	Dry	4.5	0.24	0.141	0.187
	Wet	22	4	0.064	1.35
Water/ice	Fresh	81/4	0.1–10/0.01	0.03/0.16	0.1/0.01
	Sea (33 g l^{-1}, TDS)	81/4	30 000/0.1	0.01/0.16	1000/0.01
Air	Dry	1	0	0.3	0

[a] ε_r, relative dielectric permittivity; σ, electrical conductivity; v, radar velocity; α, energy attenuation; TDS, total dissolved solids.

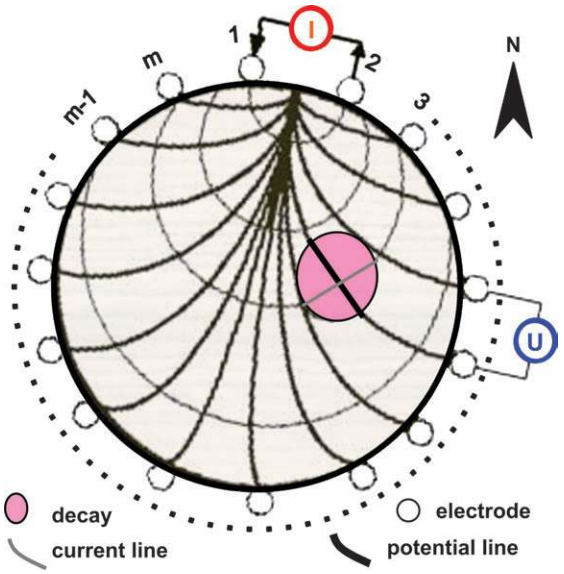

Fig. 6. Multielectrode ring array for imaging a trunk (with decay) using injected current I and measured voltage U of a dipole–dipole configuration.

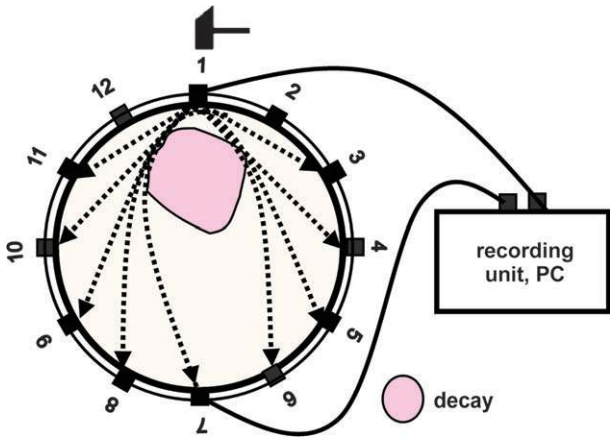

Fig. 7. Seismic tomography using a hammer source and recording transmitted elastic waves at all receivers. The curvilinear ray path around the decay shows larger travel times (lower velocities) than the rectilinear path in healthy wood.

commonly used than S-waves, which are highly attenuated (Bucur and Rasolofosaon, 1998).

Geophysical imaging tomography techniques for trunks

Traditionally, geophysical theories and techniques are developed for solving subsurface problems in (semi-)infinite earth's medium (half-/full-space) by conducting measurements from the ground surface or in boreholes. *In vivo* imaging of finite trunks (in the cm to dm range) requires special data acquisition arrays and inversion techniques that will be briefly described here.

Electric ring electrode array: A ring of needle electrodes (steel or non-polarizing saline gel) of minimum destructive nature for the study of standing trees and wood discs has been developed by Hagrey (2006) (Fig. 6). Depending on the trunk size and resolution required, an arbitrary number of electrodes are placed around the trunk's circumference. The electrodes are set carefully in contact with the tissues just below the outermost dead cork shell. The data acquisition along the ring array is carried out in analogy with that of the standard 2D pseudosections of a collinear array using electrode configurations of dipole–dipole and/or Wenner.

The measured apparent resistivity pseudosections are inverted into the true resistivity model by using a 2D iterative algorithm with finite element forward modelling (Loke and Barker, 1995; Chambers *et al*., 2003). The perfect (or imperfect) cylindrical geometry of the trunk is simulated by isoparametric quadrilateral elements with eight nodes. This allows elements with orthogonal adjacent sides of more stable numerical equations and accurate potentials.

The developed electrical imaging technique was first tested on synthetic models and laboratory trunk discs, before it was applied to many different species of healthy and stressed trees (see later). For instance, a primary ring electrode array on beech trees showed local anomalies that were related to decay occurring during the heartwood genesis (Dubbel *et al*., 1999; Weihs *et al*., 1999).

Seismic tomography of trunks: Similar to the previously mentioned data acquisition of the ring array of multielectrodes, the travel time measurements of elastic wave propagation in trunks and wood discs were also carried out at n points (n=8–32, depending on the trunk's radius, coverage, and resolution required) around the trunk's circumference (Rust, 2000), (Fig. 7). A hammer source was used for generating seismic waves at a specified point, and the travel time of waves transmitted in the medium was recorded by piezoelectric receivers at all other points. A stepwise displacement of the source to the next point and measuring travel times for all other Rx positions allowed several independent measurements of N [N=n(n−1)] for each investigated section. The Tx and Rx co-ordinates were estimated and the received signal is controlled and recorded at a PC.

The measured data sets are inverted into velocity tomograms using a simultaneous iterative reconstruction technique (Dines and

Lytle, 1979). This inversion code is based on the simulation of the pulse propagating through the medium, i.e. solving a system of linear equations iteratively.

An (ultra-)seismic tomography tool using a ring of sources and receivers has effectively localized decays with some resolution and coupling limitations, where f is unknown (Rust, 2000; Socco *et al*., 2004).

On the other hand, the application of the high resolution radar techniques has turned out to be problematic, facing poor antenna coupling and radiation, diffraction, dispersion, and attenuation (Martinis, 2002; Hagrey, 2006). Nevertheless, strong reflection events were recoded from the bark–sapwood boundary.

Hydro-/pedophysical relationships for deriving moisture content

The aforementioned backgrounds show that the electric resistivity field and radar and seismic wave propagation in soil and wood media are strongly governed by: (i) fluid content θ; (ii) salinity or total dissolved solids (TDS); (iii) density d and elastic modulus E; (iv) decay; (v) wood species and growth ring type (e.g. sap- and heartwood, late and spring wood); (vi) anisotropy; (vii) temperature T; and (viii) applied wave frequency f, causing physical property dispersion. Table 2 summarizes the effect of these factors on applied geophysical attributes.

It is clear that (di-)electric properties are dominated by θ and seismic properties by mechanical parameters d and E. Empirical and semi-/quantitative pedophysical equations link θ to ρ and v. For unsaturated vadose soils (of negligible clay content and matrix conductivity), the equation of Archie (1942) states that:

$$\rho = a\rho_w \Phi^{n-m}\theta^{-n} \tag{6}$$

where, ρ and ρ_w=bulk and water resistivity, respectively, Φ=volume fraction porosity, and a, m and n=Archie constants that depend on particle shape, sorting, cementation, etc. (Schön, 1997).

For soil sediments the equation of Topp *et al*. (1980) states that:

$$\theta = -0.053 + 0.029\varepsilon_r - 5.5\times10^{-4}\varepsilon_r^2 + 4.3\times10^{-6}\varepsilon_r^3 \tag{7}$$

where the relative dielectric constant ε_r is rewritten from equation (2) as:

$$\varepsilon_r \approx (c/v)^2 \tag{8}$$

The dielectric mixing formulae of the complex refraction index (CRIM) (Wyllie *et al*., 1956; Wharton *et al*., 1980) of the three-phase media of the vadose soil zone and trunk is given by:

$$\frac{1}{v} = \frac{(1-\Phi)}{v_g} + \frac{\Phi S}{v_w} + \frac{\Phi(1-S)}{v_a} \tag{9}$$

where v, v_g, v_w, and v_a=radar velocity of bulk medium, grain or wood, water, and air, respectively, and S_w=volume fraction saturation.

Hydrogeophysical techniques, based on these pedophysical relationships, are able to find the (static) amount of water content and even monitor its (dynamic) behaviour by repeated time-dependent measurements (time-lapses) during infiltration or growth experiments. These equations are used here to invert the geophysical attribute models in moisture distributions inside the study medium.

Geophysical imaging applications

Some examples of geophysical imaging applications at various European tree sites to study botanical and hydrological problems are presented in this section. Based on the aforementioned techniques, the individual sub-surface and trunk applications are verified by examples for mapping structures (geological bedding, single roots, root-zone, internal growth rings, and decayed wood), for monitoring processes (soil water flow, root water uptake, and sap flow), establishing pedophysical relationships, and deriving water content.

Table 2. *Factors affecting (di-)electric and seismic properties*

	DC resistivity	Radar	Seismic, P-wave
Controlling property	θ, TDS	ε, σ , μ→0	E, d
Output attribute	ρ	v, α	v, α
Controlling factors[a]			
Water content θ, salinity TDS[a]	ρ^{-1}	v^{-1}, α (ε, σ)	α (weak)
Decay, rot[a]	ρ^{-1}	v^{-1}, α (ε, σ)	v^{-1}, α
Density d[a]		v^{-1}, α (ε)	v^{-1},
Frequency f[a]	<5 Hz	v, α (ε)	v, α
Temperature T[a]	ρ^{-1}	v^{-1}, α (ε, σ)	v^{-1}, α
Wood anisotropy	$\rho_l<<\rho_r<\rho_t$	$\varepsilon_l>>\varepsilon_r>\varepsilon_t$	$v_{l>>}v_{r>}v_t$

α, energy attenuation; ρ, electrical resistivity; v, radar or seismic velocity; μ, magnetic permeability; E, elastic modulus; TDS, total dissolved solids; subscripts l, t, r are the longitudinal, transversal, and radial component, respectively.

For references, see, for example, Archie (1942); Topp *et al*. (1980); Keller and Frischknecht (1966); Simpson and TenWolde (1999); Bucur (2003, 1995); Nicolotti *et al*. (2003); Ross *et al*. (1997); Torgovnikov (1993); Sandoz (1996), Martinis (2002).

[a] These factors are directly proportional to the values given in the second, third, and fourth columns.

Geoelectrical and radar techniques for geological mapping

Field set-up and data acquisition: This example is in an olive orchard >500 years old and located in the dry region of Andria, southern Italy. Excavations in the upper 1.5 m show a thin loamy soil underlain by a weathered carbonate layer and chalky bedrock at the base. The trees are distributed at a 9×9 m^2 grid in N–S and E–W orientation. The irrigation supply, traditionally by groundwater, was supported in the last few years of dry seasons by a drip system. Hydrogeophysical experiments were conducted using electrical resistivity, radar, and TDR (time domain reflectometry) techniques to study the subsurface hydrogeology, i.e. to map the bedding as well as to determine its water content and the supply zone for the trees (see below). A team of GeoHiRes from Germany (WATER-USE partner) started the subsurface mapping by the relatively fast radar survey at a 90×60 m^2 plot. The data acquisition was carried out using a 500 MHz antenna in the vertical reflection mode of single Tx–Rx antenna offset (almost zero). Radargrams were measured along N–S and E–W grid lines with a 9 m interval. Based on radar results, geoelectric transects of apparent resistivity, 2D-pseudosections, were conducted in the Wenner and dipole–dipole electrode configurations with 0.5 m electrode spacing. Measured orthogonal pseudosections were inverted in subsurface resistivity models using the

algorithm of Loke and Barker (1995, 1996). Moreover, the lateral soil water content was monitored using TDR probes at 0.2 and 0.5 m depths below the transects.

Results: At the NE side of the site, the 3D radar data cube shows strong reflections from 0.4 m depth, indicating lateral change in the lithology and/or water content (Fig. 8a). The penetration depth of radar waves is limited to the upper 1 m, indicating a high attenuation of an electrically conductive substratum, mostly of high water saturation. The geoelectric models in the top 8 m show a thin resistive soil covering a main low resistivity layer that overlies high resistivity bedrock at the base (Fig. 8b). With increasing horizontal distance towards the NE corner, the soil cover generally increases in thickness (from 0.2 to 0.8 m) and resistivity (from 150 to 600 Ω m), whereas the TDR water content θ at 0.2 and 0.5 m depths decreases. This inverse ρ–θ relationship leads to the conclusion that humidity is the main factor governing resistivity at this site. The low resistivity layer (ρ=20–90 Ω m) of weathered, partially saturated carbonates contains the highest root density in the top 5 m and is the main water supply for the trees. The resistive base bedrock (up to >500 Ω m) is related to the parent dense chalky carbonates. Field observations show that the NE part is characterized by harder soils and small, weak trees. These findings complement and confirm each other and were proven by a follow-up excavation and sampling.

Radar tomography, reflection, and 3D electrical imaging of a root-zone

Field set-up and data acquisition: This study target of a single young poplar tree, 5 years old, is located in the Botanic Garden of Kiel, Germany. An excavation to the SE corner of the site a few days before the survey showed that the soil is characterized by heterogeneous glacial deposits of silty sand with root debris and stones. Most roots were concentrated directly under the stem; their size generally decreases with increasing depth and radial distance from the stem. The water table was at 1.2 m depth.

To map the whole root-zone envelope and to determine the soil moisture heterogeneities (see below), first a radar tomography survey was conducted in four 0.5 m deep trenches, ABCD, around the tree (Fig. 9). For each measurement, a pair of 500 MHz antennas, a transmitter Tx and a receiver Rx, was arranged in the trenches at opposite sides. For each Tx position, the direct Tx–Rx travel time was measured at all possible Rx positions. With this set-up, 2213 readings were collected with a 0.10 m interval. The measured data set was inverted into a velocity tomogram using an improved inversion algorithm that makes use of the curved raypath theory and velocity gradient zones (Hanafy and Hagrey, 2006).

For the purpose of comparing and continuing information in the 3D root zone, an electric survey was also accomplished along eight star profiles, each consisting of 32 electrodes placed at 0.2 m spacing. Apparent resistivity pseudosections were observed along each profile in the electrode configurations of Wenner and dipole–dipole. Moreover, an additional radar reflection survey was conducted to map single root branches (see below).

Results: Figures 10 and 11 show the inverted 2D radar velocity tomogram at 0.5 m depth and the geoelectric 3D model by horizontal resistivity sections with depth. In the tomogram, v generally increases with increasing radial distance from the tree. The root network of this young tree is observed as a low velocity zone (0.07–0.08 m ns^{-1}). An additional low velocity zone (0.05–0.08 m ns^{-1}) is located at the SE corner (A). This is related to higher water content of more friable and porous soils which were excavated and refilled at this corner. The strong attenuation of high f waves hindered the resolution of single roots.

In accordance with radar results, all geoelectrical sections show central negative ρ anomalies, increasing with depth and concentrating below the tree stem. Certainly, the root-zone and its water content and redistribution are responsible for these concentric low resistivities (ρ=10–30 Ω m). The SE excavation is shown by a negative anomaly.

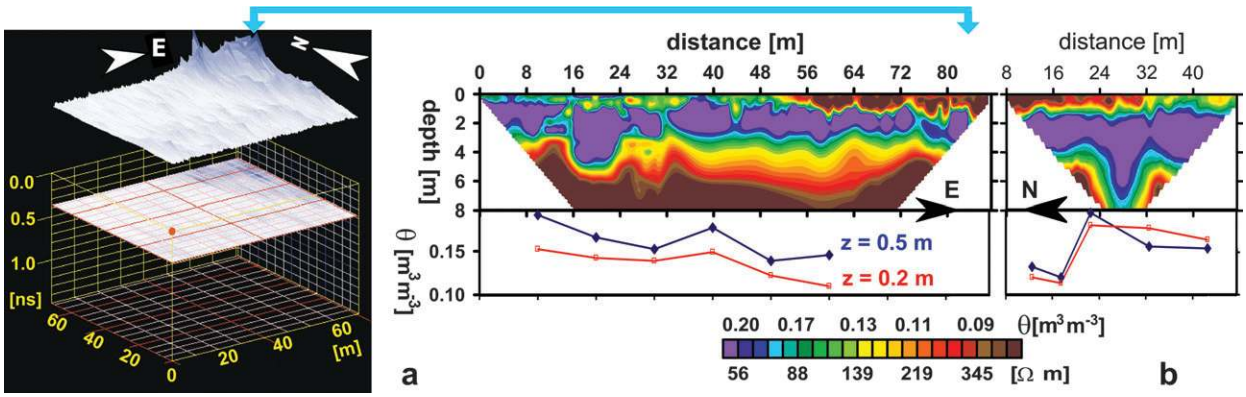

Fig. 8. Hydrogeophysical results at an olive orchard in Andria, Italy. (a) 3D radar data showing strong reflections from 0.4 m depth z in the NE corner. (b) 2D resistivity with water content θ (calculated by the equation of Fig. 13) sections and TDR θ profiles (at z=0.2 m and 0.5 m) along E–W and N–S transects crossing the site. The radar figure has been provided by GeoHiRes International Ltd, Germany.

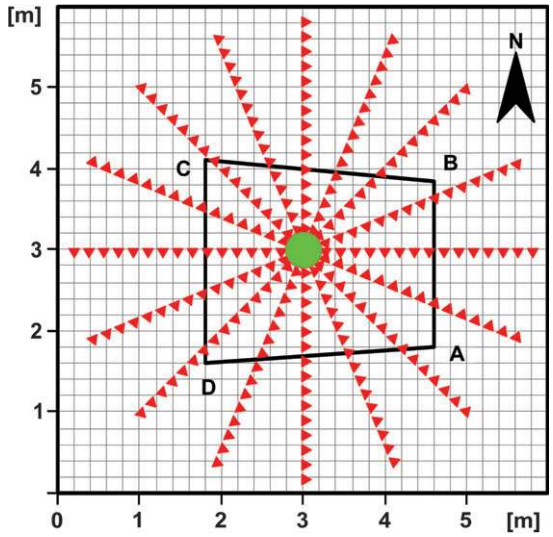

Fig. 9. Field setup around a poplar tree (green circles) of radar tomography (in a 0.5 m trench ABCD) and reflection (grid line), and star electric array (red triangles), Kiel, Germany.

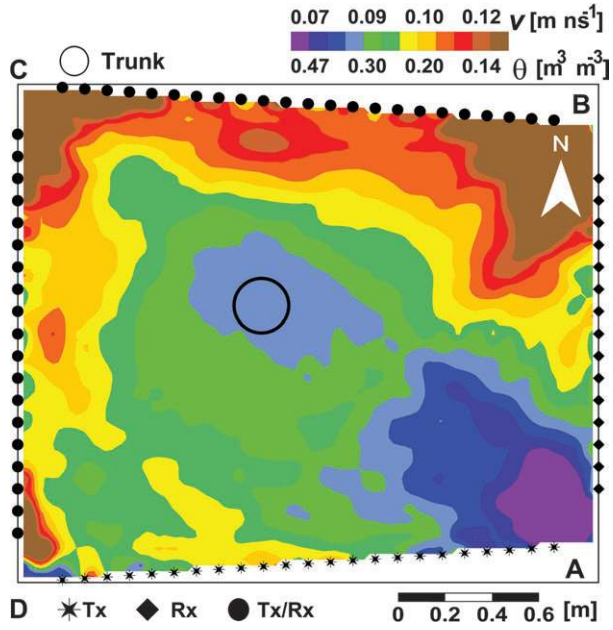

Fig. 10. 2D radar velocity tomogram resulting from the inversion of travel time measurements with a 500 MHz antenna in the trenches ABCD (Fig. 9), Kiel, Germany. θ values are derived from equations (7) and (8).

As opposed to radar, Hagrey *et al*. (2004) found that geoelectrical imaging in root-zones of old trees can even distinguish between resistive woody (water transporting) and conductive soft (absorbing) roots.

3D radar reflections from single roots

Data acquisition: For resolving single soil root heterogeneities of the same poplar tree (Fig. 9), a radar reflection

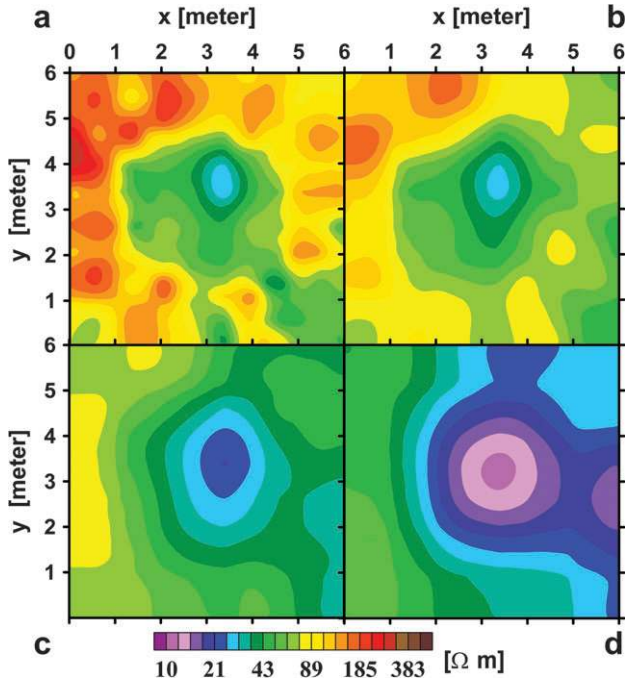

Fig. 11. Sections of a 3D resistivity model showing a negative anomaly in the root zone of a poplar tree at depths of 0.25 m (a), 0.5 m (b), 0.9 m (c), and 1.9 m (d), Kiel, Germany.

survey was accomplished over a 6×6 m^2 area around the tree. The ground survey was conducted along orthogonal grid lines at 0.2 m offset using a 500 MHz antenna in the single (almost zero) Tx–Rx offset mode. These orthogonal measurements are necessary to resolve better the elongated, small-sized root network of varying orientations, since the applied linearly polarized antenna has an azimuth-dependent ray radiation (Annan, 2004).

Results: The results are shown by a 2D radargram example and the 3D data cube of reflection and diffraction hyperbolas that were processed by an amplitude filter (Fig. 12). One can distinguish between the deep continuous reflections (R2) and the shallow single hyperbolic diffractions (R1) of irregular distribution. The R2 events with the two-way travel time of 18 ns correspond to the capillary fringe above the groundwater observed at 1.2 m depth (supposing v=0.8 m ns^{-1}, cf. the v tomogram, Fig. 10). The R1 hyperbolic diffractions reflect small-sized heterogeneities showing a relative high concentration in the centre directly below the tree stem. Thus R1 diffractions may be attributed mainly to single root branches and to a lesser extent to the coarse soil, stones, and heterogeneities. Other radar reflection mapping of roots can be found in Butnor *et al*. (2001, 2003) and Hruška *et al*. (1999).

Archie equation, subsurface water content from the resistivity model

The hydrological setting in the subsurface of the olive trees of Andria (see above) is quantified by deriving the

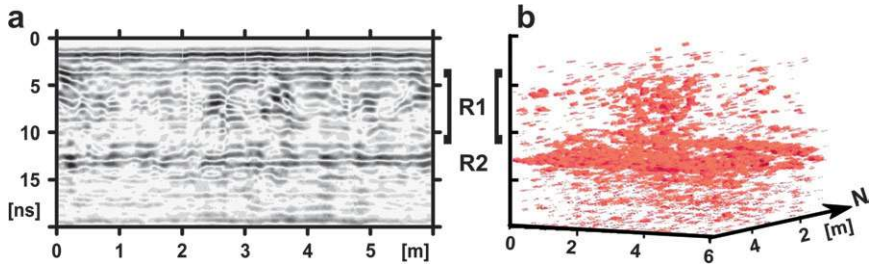

Fig. 12. Mapping single roots in a 2D radargram (a) and 3D reflections (b) using 500 MHz radar antenna in a poplar tree, Kiel, Germany. R1, single roots; R2, subsurface interface of the groundwater capillary fringe.

water content θ distributions directly from the electrical resistivity ρ models using the pedophysical Archie equation (6). The applicability of this equation here is justified by the dominance of electrolytic conductivity in the subsurface carbonates with negligible clay content. The ρ–θ relationship of Archie has been established specifically for the study site from diverse infiltration experiments, both *in situ* in the field and in the laboratory on representative soil samples of similar conditions (temperature, water, etc). The resistivity ρ was systematically determined (from modelling) as a function of θ measured by TDR probes and confirmed by gravimetric sampling (Fig. 13). The resulting best fit Archie regression, $\rho=2.05\theta^{-2.09}$ or $\theta=1.30\rho^{-0.46}$, with R^2 of 0.96, is used to transfer the resistivity models into θ models in (see legend of Fig. 8b).

The resulting θ distribution at Andria shows that the electrically resistive surface sediment and deep bedrock (ρ >400 Ω m) reflect nearly dry conditions (θ <0.09 m^3 m^{-3}), and the conductive layer (ρ <55 Ω m) shows high saturation (θ>0.2 m^3 m^{-3}). This leads to the conclusion that the high saturation horizon in the top 5 m is the main water supply for the olive trees. The wetness of this layer is related to the strong affinity of carbonates to absorb and retain infiltrating surface and rain water.

Some authors estimated θ for the subsurface by applying literature values for the parameters of the Archie equation (Turesson, 2006). These values are not specific for the sites under study and result in a rough estimate.

Topp equation and root-zone water content from a radar tomogram

The velocity tomogram of Fig. 10 was quantified in terms of water content θ using the Topp equation (7). First the tomographic *v* values were placed into equation (8) to calculate ε_r values which were then used in the Topp equation to obtain θ values directly. Hagrey *et al.* (2004) and Hagrey and Müller (2000) confirmed the applicability of the Topp equation from diverse *v* measurements as a function of θ from experiments in the field, the laboratory, and with the GeoModel. The resulting water

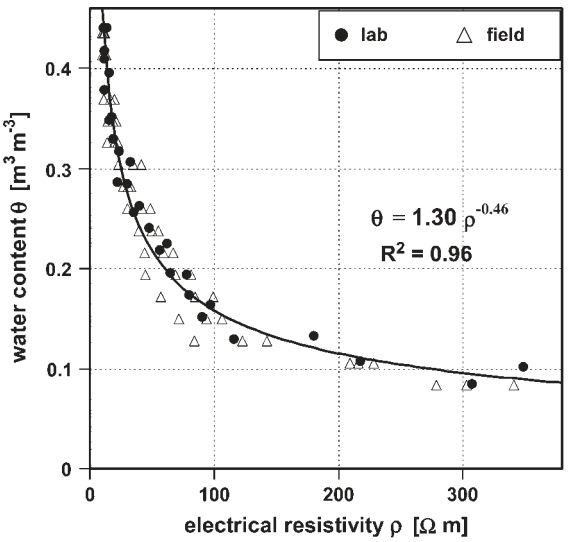

Fig. 13. Bulk resistivity ρ versus water content θ with fitting Archie's regression for olive orchard (Italy) soils from *in situ* and laboratory data.

content in the root-zone (see the legend of Fig. 10) is in the range 0.25–0.40 m^3 m^{-3}. One may note that these values are the bulk moisture content within the single root branches plus the surrounding soil (Mojid and Cho, 2004). By knowing the soil porosity values, a similar procedure can be used to derive the water content from the CRIM equation (9). Similar studies have been reported by many authors (Huisman *et al.*, 2003; Schmalholz *et al.*, 2004).

Geoelectrical monitoring root water uptake in cork oaks in Portugal

Field set-up and data acquisition: Hydrogeophysical experiments were carried out on endangered cork oak *montado* trees near Rio Frio, Portugal. The objectives were to monitor soil water variations and uptake by roots and to identify water stress zones in addition to mapping the subsurface hydrogeology. The oaks, >100 years old, grow within the Tagus valley in a Mediterranean climate with

Atlantic influence of high air humidity. The current average annual evapotranspiration exceeds the precipitation. The trees are supplied mainly by the groundwater. Excavations at the study site show that the fluvial sediments are covered by heterogeneous, loamy sand with clay intercalations that overlie cemented sand.

Time-dependent apparent measurements of resistivity pseudosections were performed along the surface and subsurface transects in the Wenner and dipole–dipole configurations at 0.07–0.5 m fixed electrode spacing. Monitored data sets were inverted using 2D time-lapse of joint dependent resistivity inversion (deGroot-Hedin and Constable, 1990; Loke, 1999). The inversion model of the initial data set is used as a reference model to constrain the inversion of the later time-lapse data sets.

Results: Figure 14 shows an example of the resulting subsurface ρ sections together with monitored anomalies $\Delta\rho$ [$\Delta\rho=(\rho_t-\rho_0)/\rho_0$; ρ_0, ρ_t=resistivity before and after time t of infiltration]. The ρ section shows a three-layer model of a middle conductive (wet) layer sandwiched by a resistive porous sandy soil of varying thickness on top, and resistive bedrock below. The middle layer (depth range=1.5–9 m) contains most roots and is the main water supply for the oaks. The single anomalies $\Delta\rho$ within the upper 2 m reflect the spatio-temporal humidity variations during 16 monitoring days. Tree areas with water uptake by roots show higher $\Delta\rho$ and dryness values than treeless areas. Werban *et al.* (2005) followed the procedures detailed in the previous section and converted resistivity models into pore water distribution.

Other applications for monitoring soil water infiltration have been reported (Hagrey *et al.*, 1999, 2004; Müller *et al.*, 2003).

Ring electrode array for imaging structure, decay, and fluids in trunks

The ring array technique (described earlier) was applied to study the healthy state of various tree species, especially endangered olives (Andria orchard, Italy) and cork oaks (Rio Frio *montado*, Portugal). Examples for mapping the internal structure and exploring the capability for detecting wood humidity and monitoring sap flow are given in this and the following sections.

Olive trunk images show the ring structure with a radial decrease of resistivity from the centre outwards (Fig. 15a–c). Compared with young trees (7-years-old), old olive trunks (>100 years old), sometimes with a central cavity, display thick, very high resistive heartwoods and thin conductive sapwoods. The asymmetry of the ring structure of a young tree on old roots (Fig. 15c) is related to its position relative to the mother tree and the influence of predominant sunlight and/or wind directions. In contrast to most studied cases, the cork oaks show central resistivity lows, sometimes even chaotic, which reflect wet heartwood of irregular, weakly defined sap–heartwood interface (Fig. 15d, e). The results were confirmed by sap flow data and core sample results. Wet heartwood with stinky outflows indicates fungal or bacterial infection which is the main reason for the oak decline observed in this plantation. Olive trees show generally drier heartwood than other studied tree species (e.g. cedar, beech, peach, and cork oak).

In a cedar tree trunk, the internal resistivity structure ρ was imaged and its gravimetric fluid content distribution θ determined on core samples extracted from the different rings (Hagrey *et al.*, 2004). The results show an inverse

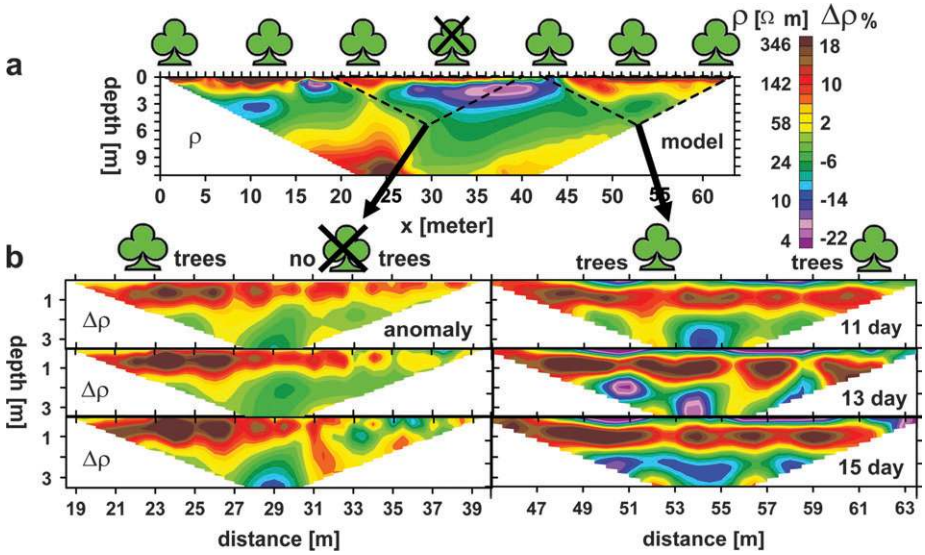

Fig. 14. Electrical resistivity model ρ (a) and time-lapse anomalies $\Delta\rho$ (b) after monitoring for 15 d (no irrigation) in a cork oak *montado*, Portugal. The low ρ layer (top 6 m, a) supplies trees with water. With time, $\Delta\rho$ and dryness increase by root water uptake in the top 2 m below trees only. Treeless areas (b) show slight changes.

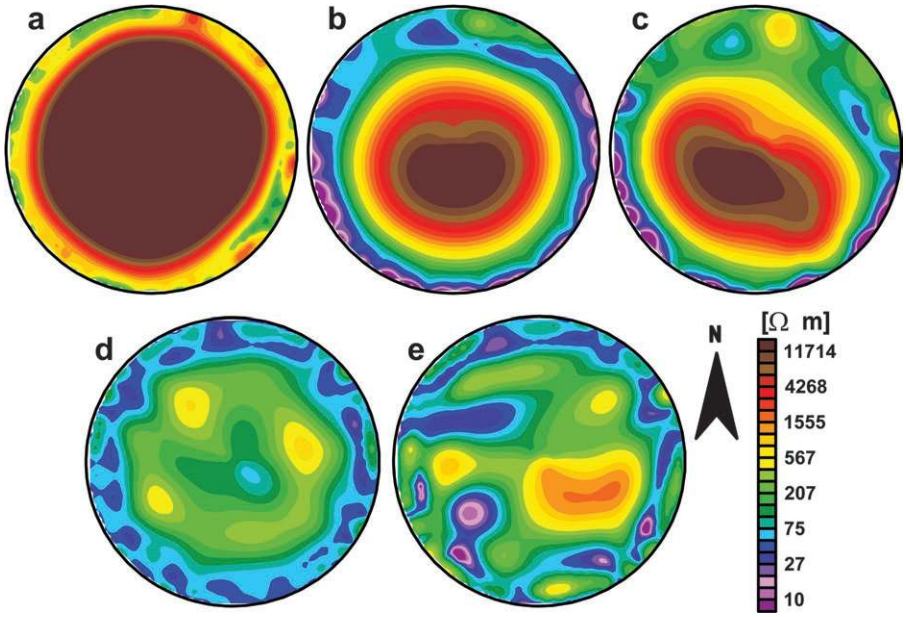

Fig. 15. 2D resistivity ρ trunk model of olive (Andria, Italy, a, b, c) and cork oak (Rio Frio, Portugal, d, e) trees. Olive images show an old tree (a, radius r=0.16 m) and two young trees, one standing isolated (b, r=0.03 m) and the other growing on roots of an old tree (c, r=0.06 m). Oak images display weakly (d, r=0.18 m) and strongly (e, r=0.23 m) infected trunks. Heartwood resistivities of olives (highest ρ in old trees with a central cavity) are much higher than those of oaks (lowest ρ in decay). The asymmetry in (c) is related to a predominant sun and/or wind direction.

linear relationship between θ and the logarithm of ρ ($\ln\rho = -4.96\theta + 5.31$), i.e. the ρ image is influenced mainly by θ variations and little by ion changes between the growth rings (Carll and TenWolde, 1996; Simpson and TenWolde, 1999).

Ring electrode array for monitoring sap flow

Field set-up and data acquisition: The investigated peach tree, 8-years-old, belongs to an orchard in Atalaia, Portugal. Trees are irrigated by a drip system and the subsurface consists mostly of cemented fluvial sand (Hagrey and Michaelsen, 2002; Hagrey *et al*., 2004). Along a trunk axis (0.1 m diameter), a linear array of 16 electrodes was installed at the outer surface at 0.01 m electrode spacing. After accomplishing reference measurements, the stained irrigation started with 1.0 l of tracer solution (3 g l^{-1} NaCl) and diluted with distilled water for 23 h. Resistance pseudosections in dipole–dipole configuration monitored the uptake process by sap flow through the trunk.

Results: Monitored images are plotted with time elapsed after the NaCl injection during the dilution (Fig. 16). The individual successive pseudosections reflect the qualitative resistivity distribution inside the trunk with progress of infiltration and time. They show at the beginning (pre-infiltration) a relatively high resistance, then an abrupt resistance decrease directly after injecting the conductive tracer, and the subsequent slow gradual resistance recovery (increase) with time due to the dilution with distilled water. The upward flow velocity of the salt tracer to the middle point of the electrode array is 0.8 cm min^{-1}. The injected tracer effect has disappeared almost 23 h after infiltration begun.

Seismic tomography for detecting trunk decay

The GeoHiRes team has conducted seismic tomography measurements using a commercial instrument (Rust, 2000; Schwarze *et al*., 2004) on some trees at sites in the olive orchard (Italy), at the cork oak *montado* (Portugal), and in the beech forest (Germany). The aim was to detect and localize wood decays and defects in trunks, as well as to compare the results with that of the ring electrode technique. Resulting velocity tomograms show that the seismic technique is sensitive to the different grades of wood degradation (Fig. 17). The velocity shows the highest values in healthy sound woods, for example, the oak tree (Fig. 17a), decreases with increasing decay grade, for example, beech and cork oak trees (Fig. 17c, d), and approaches minimum values in cavities (1200 m s^{-1}), for example, olive trees (Fig. 17b). The observed artefacts and resolution limitation (outer small light, regular patches, Fig. 17a, c) are attributed to the poor ray path coverage and sensor coupling. The seismic technique is powerful in detecting decays but it is not able to resolve the single ring structures of sap- and heartwood. This can be explained by the poor impedance contrast at the growth ring interfaces. In contrast, these growth rings possess

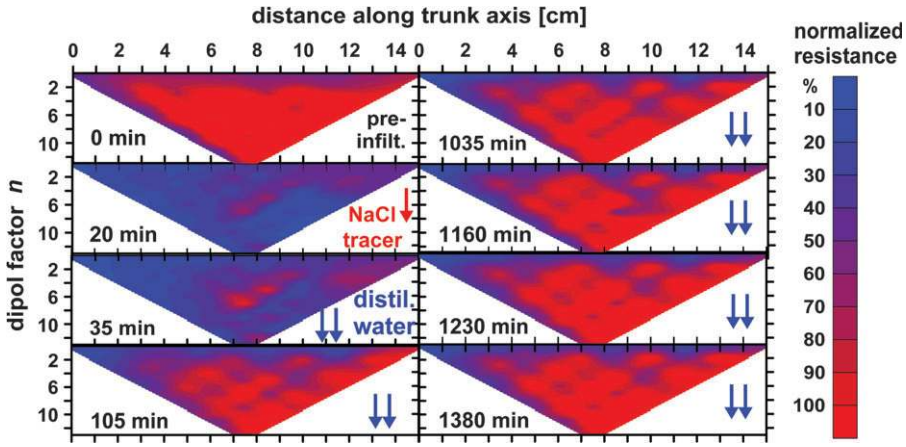

Fig. 16. *In vivo* electrical resistivity experiments on a peach tree, stained, and distilled water infiltrated to wash down an NaCl tracer (injected at the start) as a function of time. Resistance pseudosections from repeated dipole–dipole measurements (n=1–13, see Fig. 2) along an axial electrode array parallel to the trunk.

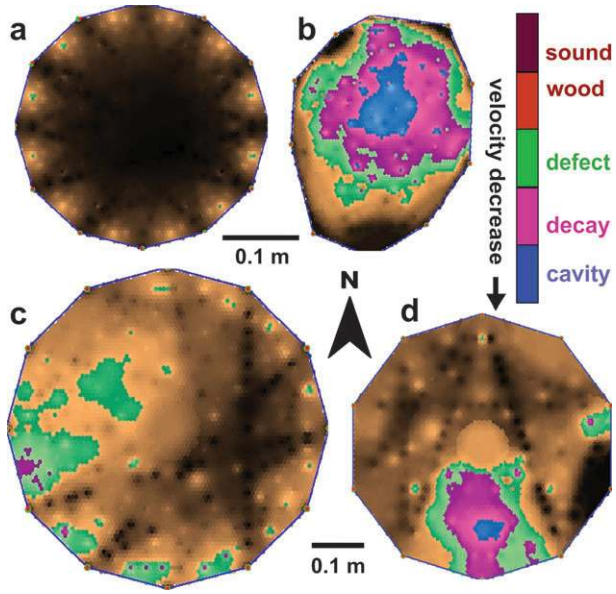

Fig. 17. Seismic velocity tomograms of tree trunks. (a) Healthy oak. (b) Olive with a central cavity. (c) Cork oak with deteriorated structure. (d) Beech with visible fungus infection. The outer small regular light patches are artefacts caused by lower ray path coverage between the transmitter and receiver. This figure has been provided by GeoHiRes International Ltd, Germany.

strong electrical contrasts resulting from water variations and, accordingly, are well resolved by the ring electrode technique. A further comparison of the seismic tomography with electrical imaging techniques is given in the next section.

Conclusion

Biotic and abiotic stresses in trees lead to changes in their physiological structures and processes, and result in productivity loss and finally in stand decline. Significant stress agents such as water extremes, salinity, and infection lead to wood decay and modifications of moisture, ion, cellulose, and lignin content, and density. These strongly influence the (di-) electrical and mechanical properties, and justify the application of non-invasive geophysical imaging techniques for assessing tree health. The electrical field and radar waves are very sensitive to moisture changes, whereas seismic waves are sensitive to mechanical stability. The high frequency radar (MHz–GHz) strongly resolves small and close targets, but has the problem of high attenuation and shallow penetration in the wet conductive root-zone and sapwood.

Electrical, radar, and seismic imaging tomography techniques have been applied at various tree sites to study the hydrogeological and physiological structures and processes within the vadose zones, root-zones, and trunks. The individual geophysical techniques are classified according to the nature of the study medium and the problem under study. The subsurface techniques use classical theories (of half-/full-space) and modified data acquisition and inversion for high resolution studies in small-scale, organic targets. For trunks, new techniques have been developed to fulfil the requirements of finite targets and the ring structures.

The studied examples show that electrical and radar techniques are able to resolve targets and structures (in 2D/3D), monitor water processes (in 4D), and derive the moisture content in the subsurface, root-zone, and trunks. The geoelectrical and radar techniques from the ground surface are able to map hydrogeological settings (bedding, water content θ, heterogeneities), single root branches, and whole root-zone envelops. Electrical techniques are able to differentiate between resistive, woody, 'transporting' roots and conducting, soft 'absorbing' roots. Both root types show low radar velocities v

Table 3. *Comparison of geophysical imaging techniques applied for studying subsurface, root-zone and trunk*

Survey	Radar (f=MHz–GHz)[a]		Electric (DC)[a]		Seismic (Hz–kHz)[a]
Technique	Reflection profiling	Transmission tomography	Subsurface imaging	Ring electrode array for trunks	Trunk tomography
Output	2D, 3D radargram	v-tomogram	2D, 3D, 4D ρ model	2D ρ model	v-tomogram
Structure studied	Hydro-geological bedding, single roots, bark–xylem interface	θ heterogeneity, root-zone	Hydro-geological bedding, root-zone, isolate absorbing from woody root-zone	Growth rings, heartwood, decay, cavity, abnormal structure	Sap–heartwood boundary, decay, cavity
Processes monitored	Soil water flow	Soil water flow	Subsurface infiltration, root uptake, root-zone redistribution, hydraulic lift	Sap flow using appropriate tracer	Hardly sensitive for flow processes
Moistures θ derived	θ model/change using semi-/quantitative Topp, CRIM equations	θ model/change using semi-/quantitative Topp, CRIM equations	θ model/change using empirical Archie equations	θ model/change using empirical Archie equations	Hardly sensitive to moisture
Advantage	Highest resolution, isolate single roots	Isolate root-zone, θ heterogeneity	Differentiate root-zone, monitor process	Resolve ring structure, all defects, monitor sap flow	Sensitive for mechanical stability
Disadvantage	Attenuation, weak penetration in wet root-zone/sapwood, no isolation of soft from woody root	Weak signals in wet zones	No resolution of single fine roots, smearing of sharp interfaces	Difficult to characterize cavities in dry heartwood	no resolution of growth rings
Resolution	cm → increases with f, coverage and contrast, decreases with α	cm → increases with f, coverage and contrast, decreases with α	cm–dm → increases with coverage (decreasing electrode spacing), contrast	cm–dm → increases with coverage (decreasing electrode spacing), contrast	cm–dm → coverage, f, α, contrast

[a] α, Attenuation; ρ, electrical resistivity; σ, conductivity; v, radar/seismic velocity; θ, water content; f, frequency.

due to their high water content. The radar surveys are able to see even single roots by generating reflection hyperbolas.

The ring electrode array around trunks can be used as a means of fast health inspection in trees, studying structures and processes. It can map the individual ring structures and isolate anomalous growths and the different types of wood defects and decays. Healthy trees show the highest resistivity ρ within central dry heartwood which decreases toward the peripheral wet sapwood. An inverse ρ–θ relationship in fresh wood is established and can be used for quantifying wood humidity from ρ images. Branching and shooting, as well as a predominant light/wind direction, result in asymmetric structures. Infections and decays cause a chaotic structure, rots develop ρ minima and cavities generate ρ maxima. Seismic tomography on the other hand is able to isolate wood decays and cavities by low v, but it can neither resolve the ring structures nor monitor sap processes. In trunks, the electrical resistivity anomalies due to moisture are much higher than the seismic velocity anomalies due to mechanical variations.

Electrical and radar techniques on the other hand are able to derive water content θ and monitor infiltration processes, for example root water uptake and sap flow by time-lapses. Radar studies are able to resolve infiltration in soils, but attenuation and coupling problems complicate the study in living trunks of high water saturation. In general, the moisture content θ can be quantified from ρ and v using empirical and semi-/quantitative pedotransfer functions established from infiltration experiments carried out in *in situ*, in the laboratory, and using the GeoModel.

Table 3 shows a brief comparison of the geophysical imaging tomography techniques applied for studying hydrogeophysical and physiological problems in the subsurface of tree sites and trunks.

Acknowledgements

A part of the presented work was carried out within the framework of the WATERUSE (EVK1-CT-2000-00079) and GeoModel (02WU0263) projects financed by the European Commission and the German Federal Ministry of Education and Research. Special thanks to Dr Andreas Kathage and Dr Susanne Kathage (GeoHiRes International Ltd, Germany) for providing data of radar at Andria, Italy, and seismic trunk tomography. Thanks to my colleagues of the working group Hydro-/Biogeophysics Dr Ulrike Werban, Professor Rolf Meissner, Professor Wolfgang Rabbel, and Ali Ismaeil for helping in data acquisition, processing, and comments, to Professor Hamlyn Jones, University of Dundee, for the critical comments on the manuscript, and together with Professor James Morison, University of Essex, for the invitation to provide this publication.

Appendix: list of symbols

Symbol	Notation
2D	Two-dimensions (of spatial mapping) along two of the coordinates (x, y, z)
3D	Three-dimensions (of spatial mapping) along the coordinates (x, y, z)
4D	Four-dimensions (of monitoring) with x, y, z, t/time
α	Energy attenuation (dB m^{-1}), the wave energy dissipated by physical characteristics of transmitting lossy (conducting) media
c	Electromagnetic wave (light) velocity in vacuum ($\approx$0.3 m ns^{-1})
CRIM	Complex refraction index method, see equation (9)
C_1, C_2	Current electrode pair for injecting current into a medium, each is a stick of metallic or non-polarizing material acting as an electric contact
d	Density (kg m^{-3})
DC	Direct current
δ	Skin depth (m) of electromagnetic waves in lossy (conducting) media, an effective penetration depth at which a wave amplitude has been attenuated by exp^{-1} (or 37%)
$\Delta\rho$	Electrical resistivity anomaly, the relative deviation of any repeated measurement from the reference resistivity data
E	Geographic East
E	Elastic modulus (N m^{-2}), describes stress–strain ratios in an isotropic medium which obeys Hook's law, see k_b and μ_s
ε	Dielectric permittivity (F m^{-1}), a material's capacity to store charge by applying an electric field
ε_r	Relative dielectric permittivity with respect to that of a vacuum (8.854×10^{12} F m^{-1})
Exp	Base of natural logarithm, ln $\approx$2.718
f	Wave frequency (Hz), f=Hz–kHz in seismic and MHz–GHz in radar
GPR	Ground-penetrating radar, an electromagnetic technique (f=MHz–GHz) to image and characterize the shallow subsurface
I	Electric current intensity (A)
k_b	Bulk or incompressibility modulus (N m^{-2}), the stress–strain ratio under simple hydrostatic pressure, see E and μ_s
λ	Wavelength (m)
μ	Magnetic permeability (H m^{-1}), the ratio of magnetic induction to inducing field strength
μ_r	Relative magnetic permeability with respect to that of a vacuum (1.257×10^{-6} H m^{-1})
μ_s	Shear or rigidity modulus (N m^{-2}), the stress–strain ratio for simple shear, see E and k_b
N	Geographic North
NaCl	Sodium chloride
Ω	Ohm, electrical resistance unit
P-wave	Primary, longitudinal, compressional or 'stress' body wave with a particle vibration in the propagation direction; it is faster than the S-wave
P_1, P_2	Potential electrode pair for measuring voltage (see C_1, C_2)
Φ	Volume fraction porosity (m^3 m^{-3}), the pore volume fraction in the bulk soil/rock sample
r	Average radius of a cylindrical trunk
R	Reflection coefficient, amplitude ratio of reflected to incident wave
R^2	Determination coefficient, reveals the fitting degree of estimated regression line/curve to the actual data points
ρ	Specific electrical resistivity (Ω m), the resistance of current flow in a medium (inverse σ)
ρ_a	Apparent electrical resistivity (Ω m) obtained from measurements in a heterogeneous medium
ρ_w	Electrical resistivity of water (Ω m), it is inversely proportional to TDS
Rx	Receiver antenna for recording electromagnetic radar waves
S	Geographic South
S-wave	Secondary transversal or shear body wave with a particle vibration perpendicular to the propagation direction
S_w	Volume fraction saturation (m^3 m^{-3}), the water volume fraction in the bulk soil/rock sample
σ	Specific electrical conductivity (S m^{-1}), inverse ρ
T	Temperature (°C)
TDR	Time domain reflectometry; a probe to estimate soil water content and conductivity from the wave velocity and amplitude of an electromagnetic pulse propagating in a medium along a guide line
TDS	Total dissolved solids or water salinity (g l^{-1}), it is inversely proportional to ρ_w
θ	Water content, volumetric (m^3 m^{-3}) or gravimetric (g g^{-1}), the water volume or mass fraction in the bulk soil/rock sample
Tx	Transmitter antenna for radiating radar waves
U	Electric voltage (V), measured between an electrode pair
v	Velocity (m s^{-1}) of radar or seismic waves in a medium
VTA	Visual tree assessment of Mattheck and Breloer (1994)
W	Geographic West

References

Annan AP. 2004. *Ground penetrating radar, principles, procedures and applications*. Mississauga, Canada: Sensors & Software.

Archie GE. 1942. The electrical resistivity log as an aid in determining some reservoir characteristics. *Transactions of the American Institute of Mining Engineers* **146,** 54–62.

Asprion U. 1998. *Ground-penetrating radar (GPR) analysis in aquifer-sedimentology: case studies, with an emphasis on glacial systems of SW Germany*. Tübinger Geowissenschaftliche Arbeiten, Reihe A, Band 43.

Beall FC. 1996. *Application of ultrasonic technology to wood and wood-based materials. 2nd International Conference on the Development of Wood Science Technology and Forestry, Sopron, Hungary.*

Bucur V. 2003. *Nondestructive characterization and imaging of wood*. New York: Springer-Verlag.

Bucur V. 1995. *Acoustics of wood*. Boca Raton, FL: CRC Press.

Bucur V, Rasolofosaon PNJ. 1998. Dynamic elastic and nonlinearity in wood and rock. *Ultrasonics* **36,** 813–824.

Butnor JR, Doolittle JA, Kress L, Cohen S, Johnsen KH. 2001. Use of ground-penetrating radar to study tree roots in the southeastern United States. *Tree Physiology* **21,** 1269–1278.

Butnor JR, Doolittle JA, Johnsen KH, Samuelson L, Stokes T, Kress L. 2003. Utility of ground-penetrating radar as a root biomass survey tool in forest systems. *American Journal of Soil Science Society* **67,** 1607–1615.

Caldwell MM. 1988. Plant root systems and competition. In: Greuter W, Zimmer B, eds. *Proceedings, XIV International Botanical Congress*. Koeltz, Germany, 385–404.

Caldwell MM, Dawson TE, Richards JH. 1998. Hydraulic lift: consequences of water efflux from the roots of plants. *Oecologia* **113,** 151–161.

Chambers JE, Loke MH, Ogilvy RD, Meldrum PI. 2003. Noninvasive monitoring of DNAPL migration through a saturated porous medium using electrical impedance tomography. *Journal of Contaminant Hydrology* **68,** 1–22.

Carll C, TenWolde A. 1996. Accuracy of wood resistance sensors for measurement of humidity. *Journal of Testing and Evaluation* **24,** 154–160.

Collinson JD, Thompson DB. 1989. *Sedimentary structures*. London: Chapman & Hall.

Dahlin T. 1996. 2D resistivity surveying for environmental and engineering applications. *First Break* **14,** 275–284.

Daniels DJ. 1996. *Subsurface penetrating radar*. London: The Institutution of Electrical Engineers.

deGroot-Hedlin C, Constable S. 1990. Occam's inversion to generate smooth, two-dimensional models from magnetotelluric data. *Geophysics* **55,** 1613–1624.

Davis JL, Annan AP. 1989. Ground penetrating radar for high-resolution mapping of soil and rock stratigraphy. *Geophysical Prospecting* **37,** 531–551.

Dawson TE, Pate JS. 1996. Seasonal water uptake and movement in root systems of Australian phreatophytic plants of dimorphic root morphology: a stable isotope investigation. *Oecologia* **107,** 13–20.

Dines KA, Lytle RJ. 1979. Computerized geophysical tomography. *Proceedings of the Institute of Electrical and Electronic Engineers (IEEE)* **67,** 1065–1073.

Dubbel VV, Weihs U, Krummheuer F, Just A. 1999. New method for 2D imaging of decay in pine. *AFZ-Der Wald* **26,** 1422–1424 (in German).

Gisi U, Schenker R, Schulin R, Stadelmann FX, Sticher H. 1997. *Soil ecology*. Stuttgart: Georg Thieme Verlag (in German).

Hagrey SAal. 2006. Electrical resistivity imaging of wooden tree trunks. *Near Surface Geophysics* **4,** 177–185.

Hagrey SAal, Meissner R, Werban U, Rabbel W, Ismaeil A. 2004. Hydro-, bio-geophysics. *The Leading Edge* **23,** 670–674.

Hagrey SAal, Michaelsen J. 1999. Resistivity and percolation study of preferential flow in vadose zone at Bokhorst, Germany. *Geophysics* **64,** 746–753.

Hagrey SAal, Michaelsen J. 2002. Hydrogeophysical soil study at a drip irrigated orchard, Portugal. *European Journal of Environment and Engineering Geophysics* **7,** 75–93.

Hagrey SAal, Müller C. 2000. GPR-study of pore water content and salinity in sand. *Geophysical Prospecting* **48,** 63–85.

Hagrey SAal, Rabbel W, Meissner R, Werban U. 2003. The 'GeoModel' at Kiel—a hydrogeophysical full scale model for Engineering Geology to study pore water, contamination and structure of soils. *Proceedings, Meeting of Engineering Geology*, Kiel, Germany, 361–362.

Hagrey SAal, Schubert-Klempnauer T, Wachsmuth D, Michaelsen J, Meissner R. 1999. Preferential flow, first results of a full scale flow model. *Geophysical Journal International* **138,** 643–654.

Hallof PG. 1957. On the interpretation of resistivity and induced polarization measurements. PhD thesis, Massachusett Institute of Technology.

Hanafy ShM, Hagrey SAal. 2006. Radar tomography for soil moisture heterogeneity. *Geophysics* **71,** k9–k18.

Hruška J, Cermák J, Sustek S. 1999. Mapping of tree root systems by means of the ground penetrating radar. *Tree Physiology* **19,** 125–130.

Hubbard SS, Grote K, Rubin Y. 2002. Mapping the volumetric soil water content of a California vineyard using high-frequency GPR ground wave data. *The Leading Edge* **21,** 552–559.

Huisman JA, Hubbard SS, Redman JD, Annan AP. 2003. Measuring soil water content with ground penetrating radar: a review. *Vadose Zone Journal* **2,** 476–491.

Keller GV, Frischknecht FC. 1966. *Electrical methods in geophysical prospecting*. Oxford: Pergamon Press.

Koefoed O. 1979. *Geosounding principles 1: resistivity sounding measurements*. Amsterdam: Elsevier Science Publishing Company.

LaMarche Jr VC. 1974. Paleoclimatic inferences from long tree-ring records. *Science* **183,** 1043–1048.

Lamb HH. 1995. *Climate, history and the modern world*. London: Routledge.

Loke MH. 1999. Time-lapse resistivity imaging inversion. *Proceedings, Meeting of Environmental and Engineering Geophysical Society, European Section*. Budapest, Hungary.

Loke MH, Barker RD. 1995. Least-squares deconvolution of apparent resistivity pseudosection. *Geophysics* **60,** 1682–1690.

Loke MH, Barker RD. 1996. Rapid least square inversion of apparent resistivity pseudosections using quasi-Newton method. *Geophysical Prospecting* **48,** 131–152.

Lowrie W. 1997. *Fundamentals of geophysics*. Cambridge: Cambridge University Press.

Martinis R. 2002. Nondestructive techniques for decay diagnosis on standing trees. PhD thesis, University of Florence, Italy.

Mattheck C, Breloer H. 1994. Field guide for visual tree assessment (VTA). *Arboricultural Journal* **18,** 1–23.

Miller RB. 1999. Structure of wood. In: *Wood handbook—wood as an engineering material*. Madison: US Department of Agriculture, Forest Service, Forest Products Laboratory, Report FPL-GTR-113, 463 pp, Chapter 2.

Mojid MA, Cho H. 2004. Evaluation of the time-domain reflectometry (TDR)-measured composite dielectric constant of root-mixed soils for estimating soil-water content and root density. *Journal of Hydrology* **295,** 263–275.

Müller M, Mohnke O, Schamalholz J, Yaramanci U. 2003. Moisture assessment with small-scale geophysics. *Near Surface Geophysics* **1,** 173–181.

Neal A. 2004. Ground-penetrating radar and its use in sedimentology: principles, problems and progress. *Earth-Science Reviews* **66,** 261–330.

Nicolotti G, Socco LV, Martinis R, Godio A, Sambuelli L. 2003. Application and comparison of three tomographic techniques for detection of decay in trees. *Journal of Arboriculture* **29,** 66–78.

Olhoeft GR. 1987. Electrical properties from 10^{-3} Hz to 10^{9} Hz—physics and chemistry. *American Institute of Physics Conference Proceeding* **154,** 281–298.

Parasnis DS. 1997. *Principles of applied geophysics*. London: Chapman & Hall.

Pellerin F, DeGroot RC, Esenther GR. 1985. Nondestructive stress wave measurements of decay and termite attack in experimental wood units. *Proceedings, 5th International Symposium on Nondestructive Testing of Wood,* Pullman, WA, USA, 319–353.

Raczkowski J, Lutomsky K, Molinski W, Wos R. 1999. Detection of early stages of wood decay by acoustic emission technique. *Wood Science and Technology* **33,** 353–358.

Richards JH, Caldwell MM. 1987. Hydraulic lift: substantial nocturnal water transport between soil layers by *Artemisia tridentata* roots. *Oecologia* **73,** 486–489.

Ross RJ, DeGroot RC, Nelson WJ, Lebow PK. 1997. The relationship between stress wave transmission characteristics and the compressive strength of biologically degraded wood. *Forest Products Journal* **47,** 89–93.

Ross RJ, Pellerin RF, Volny N, Salsig WW, Falk RH. 1999. *Inspection of timber bridges using stress wave timing nondestructive evaluation tools*. Madison: US Department of Agriculture, Forest Service, Forest Products Laboratory, Report FPL-GTR.114.

Rust S. 2000. A new tomographic device for the non-destructive testing of trees. *12th International Symposium on Nondestructive Testing of Wood*. Sopron, Hungary.

Sakai H, Minamisawa A, Takagi K. 1990. Effect of moisture content on ultrasonic velocity and attenuation in woods. *Ultrasonics* **28,** 382–385.

Sandoz JL. 1996. Ultrasonics solid wood evaluation in industrial applications. *10th International Symposium on Nondestructive Testing of Wood*. Lausanne, Switzerland, 147–154.

Sandoz JL, Benoit Y, Demay L. 2000. Standing tree quality assessments using acousto ultrasonic. In: Backhaus GF, Balder H, Idczak E, eds. *International Symposium on Plant Health in Urban Horticulture*. Braunschweig, Germany, 172–179.

Schachtschnabel P, Blume H-P, Brümmer G, Hartge K-H, Schwertmann U. 1989. *Textbook of soil science*. Stuttgart: Ferdinand Enke Verlag, (in German).

Schad KC, Kretschmann DE, McDonald KA, Ross JR, Green FW. 1995. *Stress wave techniques for determining quality of dimensional lumber from switch ties*. Madison: US Department of Agriculture, Forest Products Laboratory, Report FLP-RN-0265, 14 p.

Schmalholz J, Stoffregen H, Kemna A, Yaramanci U. 2004. Imaging of water content distributions inside a lysimeter using GPR tomography. *Vadose Zone Journal* **3,** 1106–1115.

Schön JH. 1997. *Physical properties of rocks: fundamentals and principles of petrophysics, handbook of geophysical exploration*. Amsterdam: Elsevier Science.

Shortle WC. 1982. Decaying Douglas-fir wood: ionization associated with resistance to a pulsed electric current. *Wood Science* **15,** 29–32.

Shortle WC, Smith KT. 1987. Electrical properties and rate of decay in spruce and fir wood. *Phytopathology* **77,** 811–814.

Schwarze FWMR, Rabe C, Ferner D, Fink S. 2004. Acoustic tomographic study of fungus infected trees, interpretation of acoustic tomograms. *AFZ-Der Wald* **59,** 55–60 (in German).

Simpson W, TenWolde A. 1999. Physical properties and moisture relations of wood. In: *Wood handbook—wood as an engineering material*. Madison: US Department of Agriculture, Forest Service, Forest Products Laboratory, Report FPL–GTR-113, 463 pp, Chapter 3.

Skaar C. 1988. *Wood–water relations*. Heidelberg: Springer-Verlag.

Socco LV, Sambueli L, Martinis R, Comino E, Nicoletti G. 2004. Feasibility of ultrasonic tomography for nondestructive testing of decay on living trees. *Research in Nondestructive Evaluation* **15,** 31–54.

Tattar TA, Blanchard RO. 1976. Electrophysiological research in plant pathology. *Annual Reviews of Plant Pathology* **14,** 309–325.

Telford WM, Geldart LP, Sheriff RE. 1990. *Applied geophysics*. Cambridge: Cambridge University Press.

Tkachuck RD. 1983. The little ice age. *Geoscience Research Institute* **10,** 51–65.

Tomikawa Y, Iwase Y, Arita K, Yamada H. 1990. Nondestructive inspection of wooden poles using ultrasonic computed tomography. *IEEE Transactions UFFC* **33,** 354–358.

Topp GC, Davis JL, Annan AP. 1980. Electromagnetic determination of soil water content. Measurements in coaxial transmission lines. *Water Resources Research* **16,** 574–582.

Topp GC, Watt M, Hayhoe HN. 1996. Point specific measurement and monitoring of soil water content with an emphasis on TDR. *Canadian Journal of Soil Science* **76,** 307–316.

Torgovnikov G. 1993. *Dielectric properties of wood and wood-based materials*. New York: Springer-Verlag.

Turesson A. 2006. Water content and porosity estimated from ground-penetrating radar and resistivity. *Journal of Applied Geophysics* **58,** 99–111.

Wang X, Divos F, Pilon C, Brashaw BK, Ross RJ, Pellerin RF. 2000. *Assessment of decay in standing timber using stress wave timing nondestructive evaluation tools*. Madison, WI: US Department of Agriculture, Forest Service, Forest Products Laboratory, Report FPL-GTR-147.

Weihs U, Dubbel V, Krummheuer F, Just A. 1999. The electrical resistivity tomography—a promising technique for detection of coloured heartwood on standing beech trees. *Forst und Holz* **54,** 166–170 (in German).

Wensink WA. 1993. Dielectric properties of wet soils in the frequency range 1–3000 MHz. *Geophysical Prospecting* **41,** 671–696.

Werban U, Hagrey SAal. 2005. Hydrogeophysical observation of soil moisture variations in the root zone. *Extended Abstracts, Meeting, Near Surface Geophysics, European Association of Geoscientists & Engineers,* Palermo, Italy.

Wilcox WW. 1988. Detection of early stages of wood decay with ultrasonic pulse velocity. *Forest Production Journal* **38,** 68–73.

Wharton RP, Hazen GA, Rau RN, Best DL. 1980. *Electromagnetic propagation logging*. Society of Petroleum Engineers. Paper 9261.

Wyllie MRJ, Gregory AR, Gardner LW. 1956. Elastic wave velocities in heterogeneous and porous media. *Geophysics* **21,** 41–70.